FUSED SILICA DUAL-SHELL GYROSCOPE WITH IN-PLANE ACTUATION BY OUT-OF-PLANE ELECTRODES REALIZED USING GLASSBLOWING AND THRU-GLASS-VIAS FABRICATION

Danmeng Wang[1], *Mohammad H. Asadian*[1], *Doreen Hii*[1], *and Andrei M. Shkel*[1]
[1]MicroSystems Laboratory, University of California, Irvine, CA, USA

ABSTRACT

This paper introduces a 3D Fused Silica (FS) dual-shell gyroscope (DSG) integrated with a planar electrode substrate, making the entire process compatible with a wafer-level fabrication. Utilizing a thru-glass-vias (TGV) technology, the fabricated out-of-plane electrode substrate supports DSG in-plane actuation, detection, and electrostatic compensation of the n = 2 mode, the n = 3 mode, as well as the synchronous operation of the two modes. A tuning algorithm was developed for all supported operational modalities. Gyroscope operations were demonstrated for the first time using the n = 2 and the n = 3 modes asynchronously, revealing Angle Random Walks of 0.03 and 0.083 deg/rt-hr and in run bias instabilities of 0.4 and 0.75 deg/hr.

INTRODUCTION

MEMS gyroscopes, due to their relatively small sizes and masses, are good candidates for operation in extreme environments, an example being the three-Dimensional (3D) Fused Silica (FS) hemispherical resonator gyroscopes (HRGs). HRGs are superior to their 2D counterparts [1] by incorporating a rugged structure, higher out-of-plane stiffness, and a relatively low operational frequency. This not only improves the sensor's integrity and survivability during the events of high-g shocks or intense vibrations, but it also permits the use of a lower stiffness in-plane mode, such as the n = 2 and the n = 3 wineglass modes, for high sensitivity angular rate measurements. The 3D FS dual-shell gyroscope (DSG) architecture was disclosed in [2], and the first experimental results were presented in our recent work [3], which introduced an additional outer cap shell as the double-ended anchor for the sensing element (inner vibrating shell), illustrated in Fig. 1. The outer cap shell is intended to improve structural robustness by supporting the inner device shell from both sides and to reduce the anchor stress by increasing the bonding area. Due to the high structural symmetry, the DSG can operate in either the angular rate or the whole-angle mode.

To implement the 3D FS dual-shell structures to operate as a Coriolis Vibratory Gyroscope, an assembly step is required to rigidly bond the resonator to a substrate for capacitive actuation and detection. Utilizing the 3D wineglass modes of the DSG structure, actuation of the in-plane vibration and electrostatic detection of the Coriolis-induced amplitude can be accomplished using out-of-plane electrodes [4], shown in Fig. 1. Since the integrated DSG is a more complex electromechanical system compared to a 2D MEMS sensor, assembly misalignment at any of the six degrees-of-freedom would lead to uneven capacitance of the sensor. In addition, it is more challenging to electrostatically compensate the DSG for mode-matched or near-mode-matched operations desirable for high angular rate sensitivity.

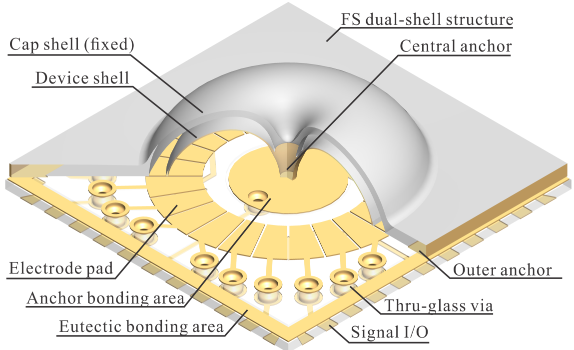

Figure 1: Schematics of a FS dual-shell gyroscope. The two layers of the shell structure were co-fabricated using the triple-stacked high-temperature glassblowing process, defining a sensing element (inner device shell), and a self-aligned fixed-fixed double-ended anchor (central stem and cap shell). A planar electrode substrate with TGVs complements the structure for electrostatic operation.

This paper describes a wafer-level TGVs fabrication process of a planar electrode substrate to be integrated with 3D FS dual-shell gyroscopes. Additionally, an electromechanical model for electrostatic frequency compensation of DSGs taking into account the effect of assembly errors was developed for mode-matched or near-mode-matched operation. Algorithms for electrostatic tuning of the n = 2 and n = 3 pairs of modes asynchronously and synchronously are presented. The angular rate measurements were experimentally demonstrated for the first time, using the n = 2 and n = 3 pairs of modes asynchronously.

FABRICATION

The planar substrate with out-of-plane electrodes for DSGs is realized by wet-etching TGVs on FS. Both the surface of the substrate and sidewalls of the vias were metalized using Cr/Au metal conductive layers to define the electrode pads, signal paths, and bonding pads. This simplifies the wafer-level fabrication process and defines high density, low parasitic interconnects with minimal mismatch between the coefficient of thermal expansion of the electrode substrate and the resonator [4].

The wafer-level process flow of the TGV electrode substrate is shown in Fig. 2. It starts with a 500 μm thick 4-inch diameter FS wafer coated with 2 μm LPCVD doped poly-silicon layers mask on both sides in preparation for isotropic wet etching, Step (a). The vias are photolithographically defined after spin-coating the FS wafer with AZ P4620 photoresist on both sides. The poly-silicon layers are then etched using a Surface Technology System (STS) Inductively Coupled Plasma (ICP) system, Step (b).

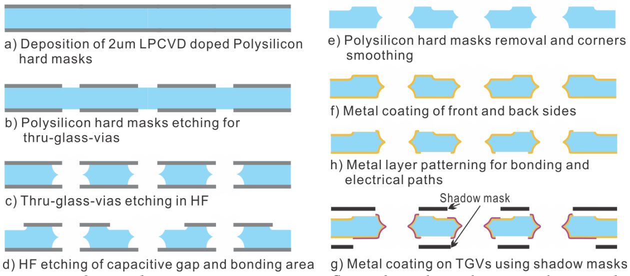

Figure 2: Fabrication process flow for the planar electrode substrate with thru-glass-vias (TGVs).

After the photoresist layer is removed, the FS wafer is time-etched to define the TGVs, etching 250 μm from both sides in an HF 48% solution, Step (c). Using another layer of photoresist, the patterns of the central and outer bonding areas for the fixed-fixed anchor architecture of the dual-shell sensor were defined on the poly-silicon hard mask of the top side of the FS wafer. The FS wafer is then wet-etched to create 40 μm cavities to reduce the capacitive gaps between the rim of the inner device shell and the planar out-of-plane electrodes, Step (d). The poly-silicon hard masks are removed completely afterwards using KOH solution. Then, the FS wafer is dipped in an HF 48% solution for 5 minutes with stirring to smooth out all corners and sharp angles prior to the metallization, Step (e). A conductive coating of 30/300 nm Cr/Au layer is deposited on each side of the FS wafer using the Denton DV-502M sputter coater, Step (f). The metal layers are then patterned using photoresist to define the central and outer eutectic bonding areas, out-of-plane electrode pads, and electrical traces, Step (h). Finally, to improve the yield of TGVs, another metal coating of 5 nm Cr and 50 nm Au is selectively deposited on each side of TGVs using two shadow masks, Step (g).

Figure 4 illustrates the front- and back-side of a TGV electrode substrate. An array of 24 planar electrodes with configurations shown in Fig. 3 is implemented on the TGV electrode substrate for flexible excitation, detection, and electrostatic frequency compensation of the n = 2 and n = 3 modes, both asynchronously and synchronously. Note that Fig. 3(c) demonstrates an example layout for synchronous operation of a DSG in the n = 2 and n = 3 modes.

ELECTROSTATIC COMPENSATION

To simulate the frequency response and electrostatic compensation of an integrated DSG, a 2-degree-of-freedom (DOF) lumped mass-spring-damper model is used. The equation of motion, including the compensating terms, in the matrix form can be represented as

$$\begin{bmatrix}\ddot{x}_n\\ \ddot{y}_n\end{bmatrix}+\boldsymbol{B}_n\begin{bmatrix}\dot{x}_n\\ \dot{y}_n\end{bmatrix}+(\boldsymbol{\Lambda_n}-\boldsymbol{\Lambda_{en}})\begin{bmatrix}x_n\\ y_n\end{bmatrix}=\begin{bmatrix}f_{xn}\\ f_{yn}\end{bmatrix}, \qquad (1)$$

where n denotes the operational mode of either $n=2$ or $n=3$ in our case. $\boldsymbol{B}_n$, $\boldsymbol{\Lambda_n}$, and $\boldsymbol{\Lambda_{en}}$ are 2×2 matrices describing the damping, elasticity, and anisoelasticity electrostatic compensation terms of the corresponding mode of DSG. x_n, y_n, f_{xn}, and f_{yn} are the displacements and forces along the X- and Y-axis. The X and Y axes of the n = 2 and n = 3 mode are determined by the directions of their corresponding forcers and pick-offs.

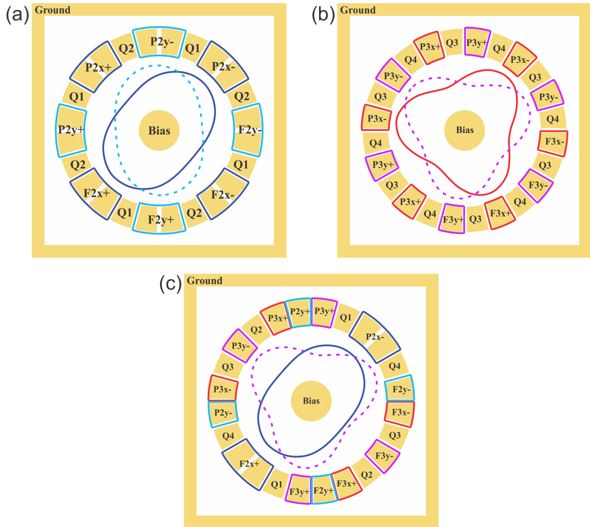

Figure 3: The electrode configurations for differential excitation and detection of (a) n = 2 mode, (b) n = 3 mode, and (c) synchronous operation of both modes for angular rate and whole angle measurements. F2x+, F2x-, P2x+, P2x-, F2y+, F2y-, P2y+, P2y-, F3x+, F3x-, P3x+, P3x-, and F3y+, F3y-, P3y+, P3y- indicate differential excitation and detection electrodes for X- and Y-axis of n = 2 and n = 3 modes, respectively. The Q1, Q2, Q3, and Q4 electrodes are for tuning and mode decoupling.

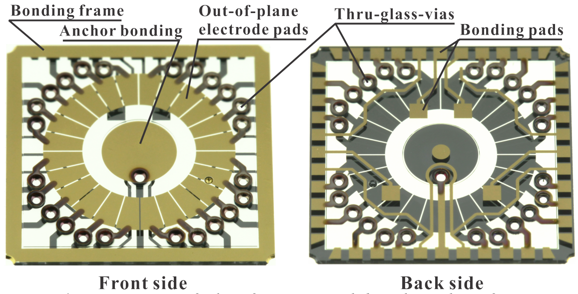

Figure 4: Images of the front- and back-side of TGV planar electrode substrate. The eutectic bonding areas (outer frame and central anchor) and electrical paths are coated with Cr/Au thin films.

To fully capture the dynamics of the assembled DSG, the effects of assembly errors introduced in the 6-DOF assembly procedure on damping, elasticity, and electrostatic compensation have to be accounted for. This is because uneven electrode gaps between the rim of the device shell and electrode substrate, as a result of assembly errors, lead to non-uniform electrostatic forces and variations of electrode capacitance at different segments of the sensing shell, thus impacting the electrostatic actuation, stiffness adjustment, quadrature coupling, and bias stability of the DSG.

Figure 5 illustrates the main assembly errors of an integrated DSG, such as the inclination between the line connecting the base of the resonator and the surface of the substrate, θ; the misalignment between centers of the dual-shell and electrode stage in the x-y plane, x_Δ and y_Δ; and φ'_δ, the azimuth angle in the shell's coordinate frame between the point of minimum gap from the shell to the substrate (δ), the center of the shell (x'_0, y'_0), and the defined X-axis of the electrode substrate (X_e). Additionally, $\theta_{\omega2}$ and $\theta_{\omega3}$ are the angles between the principal axes of elasticity of the n = 2 and n = 3 modes with X_e.

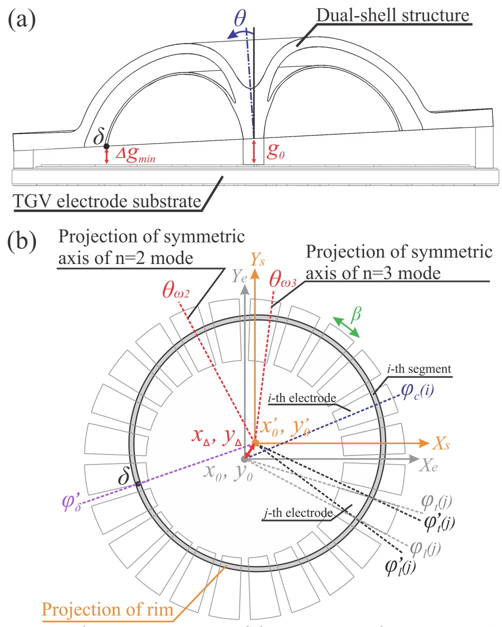

Figure 5: The main assembly errors of DSG: (a) θ and g_0 are the inclination and vertical offsets; δ is the point where the gap between the shell and the substrate, Δg_{min}, is minimum. (b) $(x_0, y_0), X_e, Y_e$ are the center coordinates, X- and Y-axis in the substrate frame; $(x_0', y_0'), X_S, Y_s$ being the equivalence in the shell coordinate frame.

The matrices $\boldsymbol{B}_n$ and $\boldsymbol{\Lambda}_n$ can be described as, [5],

$$\boldsymbol{B_n} = \begin{bmatrix} 2\mu_{\Sigma n} + 2\mu_{\Delta n}\cos(\phi) & 2\mu_{\Delta n}\sin(\phi) \\ 2\mu_{\Delta n}\sin(\phi) & 2\mu_{\Sigma n} - 2\mu_{\Delta n}\cos(\phi) \end{bmatrix}, \quad (2)$$

$$\boldsymbol{\Lambda_n} = \begin{bmatrix} \frac{1}{2}\omega_{\Sigma n}^2 + \frac{1}{2}\omega_{\Delta n}^2\cos(\phi) & \frac{1}{2}\omega_{\Delta n}^2\sin(\phi) \\ \frac{1}{2}\omega_{\Delta n}^2\sin(\phi) & \frac{1}{2}\omega_{\Sigma n}^2 - \frac{1}{2}\omega_{\Delta n}^2\cos(\phi) \end{bmatrix}, \quad (3)$$

with $\phi = 2n\theta_{\omega n}$. $\mu_{\Sigma n} = \mu_{xn} + \mu_{yn}$ and $\mu_{\Delta n} = \mu_{xn} - \mu_{yn}$ are the sum and differences of damping coefficients along the X- and Y-axis, μ_{xn} and μ_{yn}. Similarly, $\omega_{\Sigma n}^2 = \omega_{xn}^2 + \omega_{yn}^2$ and $\omega_{\Delta n}^2 = \omega_{xn}^2 - \omega_{yn}^2$, where ω_{xn} and ω_{yn} denote the resonant frequencies along the X- and Y-axis of the DSG.

The electrostatic stiffness matrix per mass, $\boldsymbol{\Lambda_{en}}$, can be written in terms of the electrical energy stored in the capacitors, U_e, and can be further described in terms of capacitance experienced at each segment of the shell resonator,

$$\boldsymbol{\Lambda_{en}} = \begin{bmatrix} \frac{\partial^2 U_e}{\partial x_n^2} & \frac{\partial^2 U_e}{\partial x_n \partial y_n} \\ \frac{\partial^2 U_e}{\partial x_n \partial y_n} & \frac{\partial^2 U_e}{\partial y_n^2} \end{bmatrix}, \; U_e = \sum_{j=1}^{24} \frac{v_t^2(j)c(j)}{2m}, \quad (4)$$

where $v_t(j)$ is the DC tuning voltage applied on the jth electrode. For each segment $j = 1, \ldots, 24$, the capacitance accounting for the in-plane misalignment between the dual-shell structure and substrate, $c(j)$, can be calculated by taking the integral along the shell segment from $\varphi_l'(j)$ to $\varphi_t'(j)$, the angles coinciding with the start and end angles of the jth substrate electrode, $\varphi_l(j)$ and $\varphi_t(j)$, [5],

$$c(j) = \int_{\varphi_l'(j)}^{\varphi_t'(j)} \frac{\varepsilon R_m w}{g_s(\varphi') - x_n\cos(n\varphi') + y_n\sin(n\varphi')} d\varphi'. \quad (5)$$

The relationship between $(\varphi_l'(j), \varphi_t'(j))$ and $(\varphi_l(j), \varphi_t(j))$ is given by

$$\tan(\varphi_p(j)) = \frac{y_\Delta + R_m\sin(\varphi_p'(j))}{x_\Delta + R_m\cos(\varphi_p'(j))}, \; p \in \{l, t\} \quad (6)$$

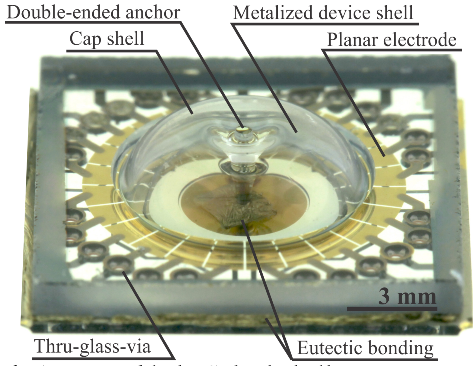

Figure 6: An assembled FS dual-shell gyroscope prototype with an array of 24 out-of-plane TGV electrode substrate.

with $\varphi_l(j) = \varphi_c(j) - \beta/2$ for the starting angle, $\varphi_t(j) = \varphi_c(j) + \beta/2$ being the ending angle, and $\varphi_c(j) = j \times \pi/12$ being the angle of the centerline of the jth electrode in the substrate frame. Variable β denotes the width of a single electrode pad. For the terms in $c(j)$, ε is the complex permittivity of air, R_m is the average radius of the device shell, and w is the width of the rim of the resonator. $g_s(\varphi')$ is the static electrode gap due to the assembly errors, $g_s(\varphi') = g_0 - \theta R_m \cos(\varphi' - \varphi_\delta')$, with g_0 being the vertical gap between the central stem and electrode. Thus, each of the second partial derivatives in $\boldsymbol{\Lambda_{en}}$ is given by

$$\frac{\partial^2 c(j)}{\partial x_n^2} = \frac{1}{2}\varepsilon R_m w \int_{\varphi_l'(j)}^{\varphi_t'(j)} \frac{2\cos^2(n\varphi')}{g_s(\varphi')^3} d\varphi', \quad (7)$$

$$\frac{\partial^2 c(j)}{\partial x_n \partial y_n} = \frac{1}{2}\varepsilon R_m w \int_{\varphi_l'(j)}^{\varphi_t'(j)} \frac{2\cos(n\varphi')\sin(n\varphi')}{g_s(\varphi')^3} d\varphi', \quad (8)$$

$$\frac{\partial^2 c(j)}{\partial y_n^2} = \frac{1}{2}\varepsilon R_m w \int_{\varphi_l'(j)}^{\varphi_t'(j)} \frac{2\sin^2(n\varphi')}{g_s(\varphi')^3} d\varphi'. \quad (9)$$

The described electromechanical model allows precise electrostatic tuning of an assembled 3D DSG by defining the appropriate tuning electrodes as well as the optimal values of the DC tuning voltages to be applied for both diagonal and off-diagonal compensations of the stiffness matrix.

EXPERIMENTAL RESULTS

A FS dual-shell resonator prototype was first characterized using a bulk piezo stack for excitation and the Laser Doppler Vibrometer (LDV) from Polytech for detection. After the structural characterization, the DSG was sputter-coated for eutectic bonding and subsequent electrostatic actuation and detection. In order to bias the proof-mass and reduce the effect of the metal resistance, [6], a thin conductive coating consisting of 3 nm Cr and 12 nm Au was deposited on the inner device shell with an electrical resistance of 1.4 kΩ. The bonding frame and the central anchor were coated with 50 nm Cr and 500 nm Au for eutectic bonding with a TGV electrode substrate, shown in Fig. 6. The experimentally measured parameters of the DSG, before and after metalization, are listed in Table 1. The in-plane misalignment of x_Δ and y_Δ for the assembled DSG prototype were directly measured optically using a Leica DM4 B microscope. Utilizing the method for static capacitance measurement and identification presented in [5], the rest of assembly errors were determined and summarized

Table 1: *Experimentally extracted parameters and assembly errors of the 3D DSG prototype*

	f (kHz)	df (Hz)	Q_x	Q_y	With metal		(μm)		ϕ'_δ	θ	$\theta_{\omega n}$
					Q_x	Q_y	g_0	x_Δ, y_Δ			
n = 2	7.93	8.2	760k	680k	390k	320k	17	26, 14	112°	0.057°	5°
n = 3	15.7	17.5	370k	405k	190k	220k					-5.3°

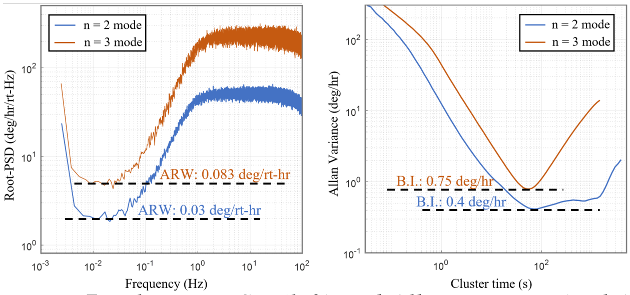

Figure 7: The root-PSD (left) and Allan variance (right) characterization of the DSG's output using either the n = 2 or n = 3 mode as the operational mode.

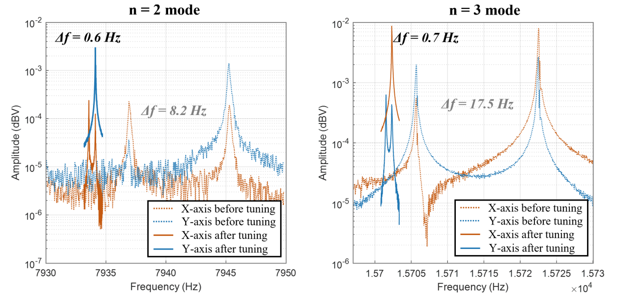

Figure 8: Frequency responses of concurrent electrostatic compensation of the n = 2 (left) and n = 3 (right) modes using the electrode configurations shown in Fig. 3(c).

in Table 1. Utilizing the electromechanical tuning algorithm, the frequency mismatches of the n = 2 and n = 3 pairs of modes were tuned separately to a value on the order of 100 mHz using the configurations shown in Fig. 3(a) and (b) with the following tuning voltages: $F_{2y} = 40.9V$, $Q_2 = 25.1V$, $F_{3x} = 61.3V$, and $Q_4 = 40.6V$. In all the experiments, the vibration amplitudes along the drive axes of the n = 2 and n = 3 modes were set to 50% of the capacitive gap and were stabilized by the AGC/PLL control loop. The closed-loop Force-to-Re-balance mode of operation was implemented in the DSG prototype for angular rate measurements. The noise performances of the DSG operation using the n = 2 and the n = 3 modes are shown in Fig. 7, revealing Angle Random Walks of 0.03 and 0.083 deg/rt-hr, and in-run bias instabilities of 0.4 and 0.75 deg/hr, respectively.

As an illustration, the frequency splits of the n = 2 and n = 3 modes of the DSG prototype were compensated concurrently to the order of 0.6 Hz using the reported tuning algorithm. The following tuning voltages were applied on the electrodes using the configuration shown in Fig. 3(c), $F_{2y} = 91V$, $F_{3x} = 96V$, $Q_1 = 12V$, and $Q_2 = 28V$. The frequency responses of the n = 2 and n = 3 modes, before and after tuning, were presented in Fig. 8 as the first step towards concurrent operations to obtain two independent measurements of the same angle of rotation for in-situ gyroscope drift compensation [7].

CONCLUSIONS

Angular rate measurements of an integrated 3D Fused Silica dual-shell gyroscope (DSG) were realized using the proposed wafer-level thru-glass-vias (TGVs) planar electrode substrate. The electrostatic compensations of the n = 2 and n = 3 pairs of modes of the 3D DSG were achieved asynchronously and synchronously using the electromechanical tuning algorithm proposed in the paper. The gyroscope operations of asynchronous n = 2 or n = 3 mode were demonstrated, and the noise performance of the DSG was presented for the first time. The array of 24 planar electrodes and the tuning algorithm open up an opportunity for flexible usage of a single and multiple pairs of modes of DSGs for in-situ calibration of gyroscopes.

ACKNOWLEDGEMENTS

This material is based on work supported by the DARPA grant N66001-16-1-4021. Devices were designed and characterized at UCI Microsystems Laboratory and fabricated at UCI INRF cleanroom facility.

REFERENCE

[1] D. M. Rozelle, "The hemispherical resonator gyro: From wineglass to the planets," in *AAS/AIAA Space Flight Mechanics Meeting*, Savannah, GA, USA, Feb. 8-12, 2009.

[2] A. M. Shkel, M. H. Asadian Ardakani, and Y. Wang, "Fused quartz dual shell resonator and method of fabrication," US20200309527.

[3] M. H. Asadian, D. Wang, Y. Wang, and A. M. Shkel, "3D dual-shell micro-resonators for harsh environments," in *IEEE/ION Position, Location and Navigation Symposium (PLANS)*, Portland, Oregon, USA, April 20 - 23, 2020.

[4] D. Senkal, M. J. Ahamed, M. H. Asadian, S. Askari, and A. M. Shkel, "Out-of-plane electrode architecture for fused silica micro-glassblown 3-d wineglass resonators," in *IEEE Sensors Conference (SENSORS)*, Valencia, Spain, Nov. 2-5, 2014.

[5] Z. Wei, G. Yi, Y. Huo, Z. Qi, and Z. Xu, "The synthesis model of flat-electrode hemispherical resonator gyro," *Sensors*, vol. 19, no. 7, p. 1690, 2019.

[6] D. Wang, W. Guan, M. H. Asadian, and A. M. Shkel, "Effect of metallization on metal-coated fused silica dual-shell gyroscopes," in *IEEE International Symposium on Inertial Sensors and Systems (INERTIAL)*, Avignon, France, March 28-31, 2022 (submitted).

[7] H. H. Ge, A. H. Behbahani, and R. T. M'Closkey, "Mems gyro drift compensation using multiple rate measurements derived from a single resonator," in *IEEE/ION Position, Location and Navigation Symposium (PLANS)*, Monterey, CA, USA, April 23-26, 2018.

CONTACT

* D. Wang, tel: +1-949-491-3559; danmenw@uci.edu